

Chapter 2

Strongly Coupled Organic Microcavities

Paolo Michetti, Leonardo Mazza and Giuseppe C. La Rocca

Abstract The photophysics of planar microcavities which employ organic materials as the optically resonant medium to achieve the strong-coupling regime is discussed. While as a result of the light–matter coupling, cavity polariton branches appear which are analogous to those observed in inorganic microcavities, many properties of organic-based microcavities are qualitatively and quantitatively different. The electronic excitations involved are molecular Frenkel excitons, rather than large radius Wannier excitons, which lead to large Rabi splitting values. The effects of disorder are typically much more pronounced as well as the exciton-phonon coupling, possibly leading to vibronic replicas. As a consequence, polariton relaxation and polariton-polariton scattering mechanisms also show features specific to the organic material employed. The field of organic-based microcavities is attracting an increasing interest as high excitation density phenomena such as polariton lasing have recently been reported. In view of their experimental relevance, two different kinds of organic microcavities, disordered J-aggregate-based microcavities and crystalline anthracene microcavities, are considered.

2.1 Introduction

The effort to improve the performance of optoelectronic devices drives the ongoing research of novel materials and architectures. In order to tame the light–matter interaction, while, on the one hand, compounds with improved linear and

P. Michetti (✉)

Institut für Theoretische Physik, Technische Universität Dresden, 01062 Dresden, Germany
e-mail: paolo.michetti@tu-dresden.de

L. Mazza

NEST, Scuola Normale Superiore and Istituto Nanoscienze—CNR, 56126 Pisa, Italy
e-mail: leonardo.mazza@sns.it

G.C. La Rocca

Scuola Normale Superiore and CNISM, Piazza dei Cavalieri 7, 56126 Pisa, Italy
e-mail: larocca@sns.it

nonlinear optical properties have been synthesized, on the other hand, dielectric microstructures have been developed engineering the photonic dispersion law and density of states (DOS), a paramount instance being photonic crystals. Rather than tailoring each of the two players—matter and light—individually to stretch the rules that govern their interaction, an alternative approach is to blend them together into hybrid entities—the polaritons—exhibiting novel potentialities.

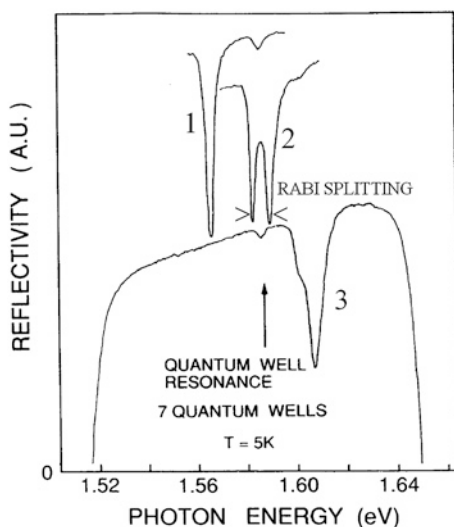
This is precisely what happens in a high finesse microcavity (MC) in which the cavity mode is resonant with a narrow electronic excitation such that their coupling overcomes the damping mechanisms. In this strong-coupling regime, the relevant eigenmodes are no longer photons and the excitons individually, but rather their coherent superpositions, i.e., the lower polariton (LP) and the upper polariton (UP) modes, which become the key players.

2.1.1 Inorganic Microcavities

Strongly coupled MCs based on inorganic semiconductors have been investigated since the early 1990s culminating with the recent observation of macroscopic quantum coherent effects such as Bose-Einstein Condensation (BEC) of cavity polaritons (see, e.g., the reviews in [1–3]). The polariton notion in bulk crystals is a traditional one [4], and in inorganic semiconductors, it comprises both the case of exciton-polaritons, wherein the matter excitation is a large radius optically allowed Wannier exciton [5], and of phonon-polaritons, wherein the matter excitation is an optical phonon in a polar lattice [6]. Bulk polaritons are characterized by a conserved three-dimensional (3D) wave vector and are not easily accessible experimentally. In typical planar microcavities, instead, a quantum well exciton is coupled to a cavity photon, and cavity polaritons are characterized by a two-dimensional (2D) in-plane wave vector. In particular, if the cavity mode cutoff energy at vanishing in-plane wave vector is lower than the exciton energy (i.e., for a negatively detuned cavity), for increasing in-plane wavevectors, the cavity photon steep dispersion and the flat exciton dispersion would cross each other, but in the strong-coupling regime, the UP and LP branches do anticross: Their separation is the Rabi splitting, proportional to the square root of the exciton oscillator strength (OS).

The MC mirrors which are usually distributed Bragg reflectors are not totally reflecting and the cavity polaritons are very weakly coupled to the 3D free-space photons having a matching in-plane wave vector and a vertical wave vector (which is not conserved) dictated by energy conservation. Injection and detection of cavity polaritons can thus be directly accomplished via angle-dependent spectroscopy, and angle-resolved reflectivity spectra are routinely employed to map the cavity polariton dispersion. The typical signature of the strong-coupling regime is a doublet of reflectivity dips, as first observed by Weisbuch et al. [7] (see Fig. 2.1).

Fig. 2.1 Low-temperature reflectivity of a strongly coupled MC containing 7 GaAs quantum wells. The three spectra correspond to different cavity detunings: Spectrum 2 is on resonance and directly shows the Rabi splitting (Adapted from [7], Copyright 1992, with the permission of The American Physical Society)



While bulk polaritons have a lower branch with an energy linearly vanishing at small wave vectors, cavity polaritons have a lower branch with a minimum energy (which for a resonant cavity is the cavity mode cutoff energy minus half the Rabi splitting) and in its vicinity, a parabolic dispersion with a very small mass, determined by the steep cavity mode dispersion, which flattens out as soon as the in-plane wave vector increases. Cavity polaritons behave as bosonic particles and, differently from free photons in vacuum, have a finite lifetime (due to leakage through the mirrors and exciton non-radiative recombination) and mutual interactions (due to the exciton-exciton scattering). Under resonant or non-resonant pumping, a bosonic-stimulated buildup of cavity polaritons at the bottom of the LP branch may occur leading eventually to a Bose-Einstein condensate—as first observed by Kasprzak et al. in 2006, see Fig. 2.2—and to superfluidity. From the technological viewpoint, interest in such phenomena has also been triggered by polariton lasing whereby the light emitted through the cavity mirrors inherits the coherence properties of the polariton ensemble. The field of inorganic-based MCs has flourished in recent years, and important new results keep being reported.

2.1.2 Organic and Hybrid Microcavities

An intrinsic limitation of inorganic-based MCs is the weak binding energy of Wannier excitons and their small OS leading to Rabi splitting values typically of the order of 10 meV. Much larger Rabi splitting values have been anticipated for MCs based on molecular Frenkel excitons [9] and already in the pioneering experiment by Lidzey et al. [10], a Rabi splitting as large as 160 meV has

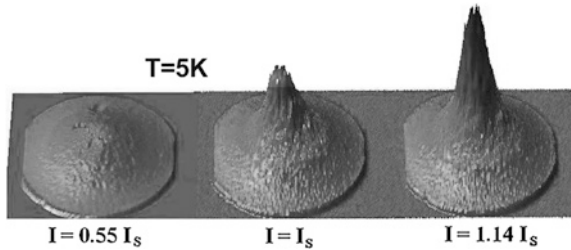


Fig. 2.2 Low-temperature angular distribution of light emitted by the LPs in a CdTe-based MC within a 23° cone around the normal direction following non-resonant excitation. The three spectra from *left to right* correspond to an excitation power below, at and above the threshold intensity I_s for BEC, the latter case being dominated by the emission from polaritons with a vanishing in-plane wavevector. (Adapted from [8], Copyright 2006, with permission of Macmillan Publishers Ltd: Nature)

been observed [10] employing a porphyrine molecule (4TBPPZn) blended in a polystyrene film as optically resonant material at room temperature. Since then, strongly coupled MCs have been demonstrated using a variety of organic materials (see, e.g., the reviews in [11–13]) which can be either classified as non-crystalline, e.g., J-aggregate blends, or (poly)crystalline, e.g., naphthalene and anthracene [14]. The knowledge accumulated for inorganic MCs can only partially be useful to understand organic MCs because, in particular, disorder effects and the electron–phonon interaction are much stronger [4, 14]. While the field of organic-based microcavities has not yet reached a maturity comparable to that of inorganic ones, very recently manifestations of nonlinearities and bosonic stimulation of organic cavity polaritons have been reported and attracted much attention [15–17].

The strategy of combining in the same MC organic and inorganic optically resonant media has also been fruitfully pursued to realize hybrid cavity polaritons [18, 19] as earlier theoretically suggested [9]. Organic–inorganic systems may capitalize on the best properties of either constituent, such as the large OS and quantum yield of organics on the one hand and the good electrical injection and transport properties of inorganic semiconductors on the other one. In strongly coupled hybrid MC, the cavity mode and both the Frenkel and Wannier excitons coherently mix so that the hybrid cavity polaritons share the properties of both of them.

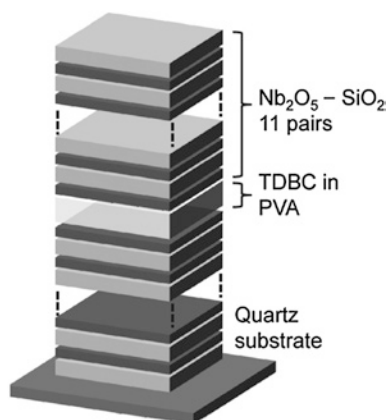
Hybrid systems and MCs have been reviewed in [13]. Here, our current understanding of organic microcavities is discussed considering as illustrative examples of non-crystalline and crystalline systems disordered J-aggregate MCs and crystalline anthracene MCs, respectively, because of their experimental relevance. The field indeed appears ripe for further theoretical and experimental developments which promise to rival those of inorganic MCs.

2.2 Amorphous J-Aggregate Microcavities

J-aggregates thin films represent the most commonly employed class of amorphous organic optically active materials for the realization of strongly coupled systems [20–22]. J-aggregates are obtained as a result of the aggregation of specific organic dyes (i.e., cyanine dyes) in polar solvents, under appropriate conditions. Upon aggregation, the optical features of the system spectacularly change into narrow and intense absorption and emission lines characterized by a very weak Frank-Condon shift, due to the rigidity of the molecular chain. These optical features are well understood as a manifestation of superradiance phenomena typical of one-dimensional Frenkel exciton systems [23]. At sufficiently low concentration, in order to avoid strong inter-aggregate interaction (and therefore the broadening of the resonance line), J-aggregates are randomly arranged in an inert host matrix. Because of their optical features, such organic materials are ideal for the observation of strong light–matter coupling. A concrete example for a J-aggregate MC structure is presented in Fig. 2.3.

The following discussion is meant to provide an introduction to the physics of J-aggregate MCs. In Sect. 2.2.1, we more broadly discuss the effect of disorder in amorphous MCs, analyzed with a minimal model [24], where an inhomogeneously broadened ensemble of two-level chromophores undergoes strong light–matter coupling. In Sect. 2.2.2, we present a theoretical model [25] of the photo-excitation dynamics of J-aggregate MCs under non-resonant pumping. This model is particularly instructive, because it allows the simulation of the photoluminescence (PL) of an organic MC, starting from a microscopical description of the bare optically active material.

Fig. 2.3 Example of an experimental structure of a J-aggregate MC consisting of a 220-nm-thick layer of TDBC J-aggregate dispersed in a polyvinyl alcohol matrix between two niobia–silica distributed Bragg reflectors (DBRs) of $11\lambda/4$ pairs. (Adapted from [26], Copyright 2011, with permission of WILEY-VCH Verlag, Advanced Functional Materials)



2.2.1 Disorder Effects

In organic-based MCs, the optically active electronic resonances are quite different with respect to the inorganic ones, being molecular excitations rather than large radius excitons. In particular, due to electron–phonon interaction or disorder scattering the molecular Frenkel excitons may behave as incoherent (diffusive) excitations rather than Bloch plane waves having a well-defined wave vector and group velocity [27]. Moreover, excitons in molecular amorphous materials, such as J-aggregate dispersed in an host matrix, are by their nature localized within a molecular aggregate with typical extensions around tens of nm. It is only the light–matter interaction that, in strong-coupling, polarizes the medium giving birth to delocalized polaritons with a well-defined wave vector. Therefore, amorphous organic films intrinsically introduce excitonic disorder of orientational, positional, and diagonal kind in the strongly coupled system. The molecules are in fact randomly arranged in the host matrix, at least at low concentration, where ordering phenomena do not arise (such as liquid crystal arrangements). Each molecule feels a different environment, thus their molecular resonance energies are shifted with respect to their average transition energy, resulting in a static inhomogeneously broadened excitonic resonance, also at low temperature. At finite temperature, dynamical disorder, due the presence of vibrations, can also contribute to the inhomogeneous linewidth. Structural disorder scattering breaks the translational invariance and the *coherence* (in this context, a coherent state is a delocalized plane-wave-like state of definite momentum) imposed by the medium polarization due to light–matter interaction, bringing about localized states quite different from plane-wave-like polaritons [24, 28]. On the other hand, orientational disorder restores a macroscopic rotational symmetry in the plane of the film, which is generally absent in an organic crystalline environment, characterized, instead, by a strong anisotropy of the optical features.

A macroscopic approach to disorder consists in solving Maxwell equations for a transverse electromagnetic wave in presence of a broad and dispersionless excitonic resonance [4, 28]. This provides a first insight on the effect of disorder in a strongly coupled system. The equation for a wave of in-plane momentum q and frequency $\omega = E/\hbar$ assumes the form

$$[E - E_{\text{ph}}(q)](E - E_{\text{ex}} + i\gamma_{\text{ex}}) = \Delta^2/4, \quad (2.1)$$

with the Rabi splitting $\Delta^2 = \frac{f_{\text{ex}}}{4\varepsilon_b}$, being f_{ex} the OS of the excitonic resonance line at energy E_{ex} and ε_b the background dielectric constant, where $E_{\text{ph}}(q)$ is the dispersion of the cavity mode and γ_{ex} the total broadening of the excitonic resonance. Equation (2.1) is solved for the real energies, giving the UP (sign +) and LP polariton (sign −) dispersion curves $E_{\pm}(q)$ [see (2.9)], and for their imaginary part $\delta E_{\pm}(q)$, accounting for the energy uncertainty. One obtains that the energy uncertainty $\delta E_{\pm}(q) = \gamma_{\text{ex}} C_{\pm}^{(\text{ex})}(q)$ is simply proportional to the exciton content of the polaritonic state [see (2.8)]. For a given wave vector, the momentum uncertainty can be quantified through the group velocity

$$\delta q_{\pm}(q) \approx \delta E_{\pm}(q)/\hbar v_{\pm}(q) \quad (2.2)$$

$$v_{\pm}(q) = \frac{1}{\hbar} \frac{dE_{\pm}(q)}{dq}, \quad (2.3)$$

and regions where polaritons possess quality of ‘good’ quasi-particles must satisfy $\delta q < q$. This procedure allows to determine a minimum and a maximum endpoint on the LP branch. Inside this range, polaritons have a coherent (delocalized) nature, while polariton localization occurs outside this region. Similarly, a minimum endpoint is defined for the UP branch, above which polaritons have a coherent nature.

Numerical and analytical results [24, 29–32] have confirmed the validity of the macroscopic model (see the following discussion in this section) and analyzed the effect of different kinds of structural disorder. Special attention has been given to the case of the disorder scattering at the bottom of the LP branch that, possessing small group velocity, is especially susceptible to suffer localization. Evidences of localized polaritons in J-aggregates have been found analyzing the reflectivity and luminescence spectra, in which a third peak between the UP and the LP branches appears [33]. This third emission peak at energy near the bare exciton resonance is found at all external angles and, being the angle related to the in-plane wave vector, we can associate it to states of high wave vector uncertainty, therefore localized for the uncertainty principle.

Now, following [24], we set up a minimal quantum mechanical model for a one-dimensional MC of length L . The MC contains two kinds of one-excitation states: N localized excitons (two-level chromophores) placed at sites r_i and delocalized photon modes, coupled by the light–matter interaction. The system is described by the model Hamiltonian (neglecting all damping processes)

$$H = \sum_q E_{\text{ph}}(q) c_q^{\dagger} c_q + \sum_j E_j b_j^{\dagger} b_j + \sum_{q,j} \left(V_{j,q} c_q^{\dagger} b_j + \text{h.c.} \right) \quad (2.4)$$

$$V_{j,q} = \frac{\Delta}{2\sqrt{N}} e^{-iqr_j}, \quad (2.5)$$

where c_q is the annihilation operator for a photon of in-plane momentum q and b_j the annihilation operator acting on the molecular exciton at the j -th site. The excitonic energies E_j have a random Gaussian distribution around their average value E_{ex} , with standard deviation σ . We apply cyclic boundary conditions for the photons so that allowed wavevectors are $q = 2\pi n/L$ with $n \in \mathbb{N}$. A direct diagonalization gives us access to the polariton eigenmodes of the system (which we arbitrarily define as the modes having a photon content larger than 5 %), which we can then completely analyze.

In an ideal situation $E_j = E_{\text{ex}}$ and $r_j = jL/N$ for $j = 0, 1, \dots, N-1$, after introducing the momentum basis for the exciton operators

$$b_q = \sum_j \frac{e^{-iqr_j}}{\sqrt{N}} b_j, \quad (2.6)$$

the system eigenstates are described by ideal cavity polaritons (ICPs)

$$p_{q,\pm} = C_{\pm}^{(\text{ex})}(q)b_q + C_{\pm}^{(\text{ph})}(q)c_q, \quad (2.7)$$

where the exciton and photon content is given by the Hopfield coefficients

$$\begin{aligned} C_{\pm}^{(\text{ex})}(q) &= \frac{\Delta/2}{\sqrt{\Delta^2/4 + [E_{\pm}(q) - E_{\text{ex}}]^2}} \\ C_{\pm}^{(\text{ph})}(q) &= \sqrt{1 - [C_{\pm}^{(\text{ex})}(q)]^2} \end{aligned} \quad (2.8)$$

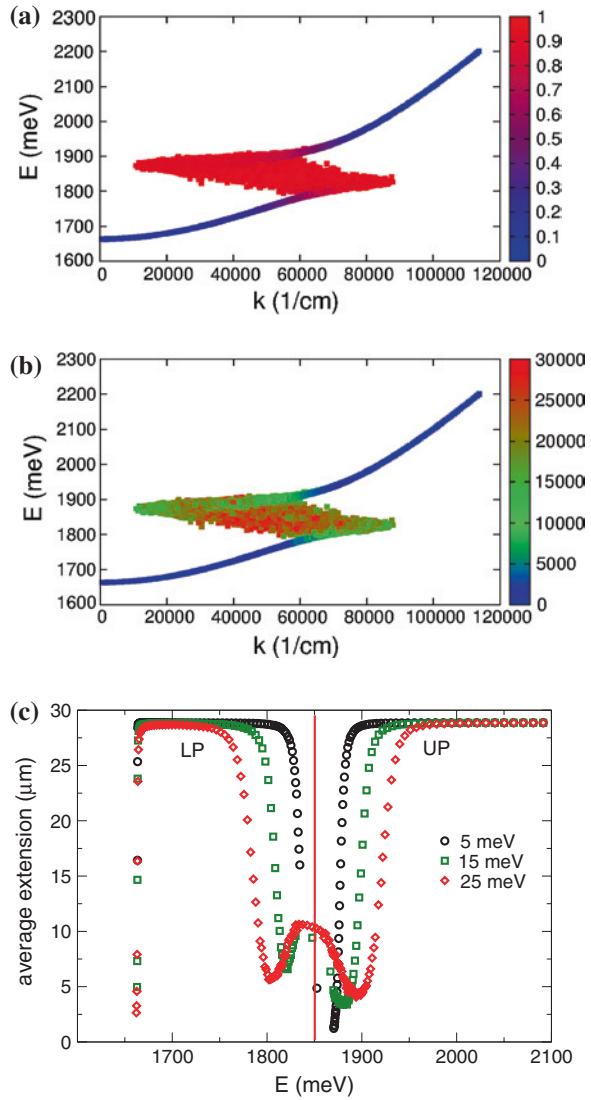
and the corresponding eigenenergies are

$$E_{\pm}(q) = \frac{E_{\text{ex}} + E_{\text{ph}}(q)}{2} \pm \frac{1}{2} \sqrt{[E_{\text{ex}} - E_{\text{ph}}(q)]^2 + \Delta^2}. \quad (2.9)$$

In Fig. 2.4a, b, we present the analysis of the eigenstates for a single realization of the model in (2.5) with on-site energetic disorder. Plotting the eigenenergies against the average wave vector (calculated on the photonic component of the eigenstates) of eigenstates with photon component larger than 5 %, we easily identify the upper and LP branches. Between the two branches, we note the presence of a large number of eigenstates, corresponding to energies similar to the bare excitation energy of the chromophores. Plotting the excitonic content of the eigenstates (in Fig. 2.4a), we note that such states are mostly exciton-like. The analysis of the standard deviation of the wave vector calculated on the photonic component [in Fig. 2.4b] reveals that these states have an incoherent nature (they do not have a well-defined momentum). Experimentally, this is consistent with the measurement of a PL peak for frequencies between the polariton branches, persisting at all observation angles [33]. In Fig. 2.4c, we plot the mean extension of the polaritonic states averaged on 5,000 disorder configurations. This analysis confirms the existence of localized states with finite exciton–photon mixing between the two polariton branches (at energies near the bare exciton resonance) and at the bottom of the LP branch, and hence the validity of the previously discussed macroscopic approach.

Now, we analyze in more detail the polariton localization at the LP bottom induced by excitonic disorder, in view of its importance for polariton condensation experiments. In Fig. 2.5, we show the mean eigenstate extension versus their energy of the four lowest lying polariton states, for an ensemble of 1,000 disorder configurations with $\sigma = 5, 10, 15$, and 20 meV. In the $\sigma = 5$ meV panel, we can indeed distinguish that the eigenstates are separated in four groups of increasing energy. For larger σ , it is instead no more possible to clearly distinguish the four eigenstates, because they form a dispersed cloud, which extends toward lower energies and increased localization values for increasing σ .

Fig. 2.4 Analysis of the eigenstates of a system of $N = 1,000$ chromophores of average on-site energy $E_{\text{ex}} = 1,850$ meV and standard deviation $\sigma = 20$ meV in a 1D MC of length $L = 10^{-6}$ m realizing a Rabi splitting $\Delta = 120$ meV. **a** Color plot of the excitonic fraction of each eigenstates plotted against the average wave vector calculated on its the photonic part. **b** Standard deviation on the average wave vector calculated on the photonic part of the eigenstates. **c** Mean extension of the (polariton-like) eigenstates having photonic fraction $> 5\%$, averaged on the spectral intervals and on an ensemble of 5,000 disorder configurations, for systems with $\sigma = 5, 10$ and 20 meV



In order to better understand the mechanism that rules the localization of the lowest energy state, we now build a simplified analytical model for the LP bottom state in presence of a single exciton defect. Let us consider a model Hamiltonian (2.5), where all chromophores have the same excitation energy E_{ex} with the exception of a single defect in the origin of the real space, with the excitonic potential energy is given by $E_{\text{ex}} - \sigma R \delta(x)$, with R the nearest neighbor distance being. We work on the reciprocal ICP space [span by (2.7)] near the bottom of the LP branch, for which the dispersion curve can be well captured by an effective mass

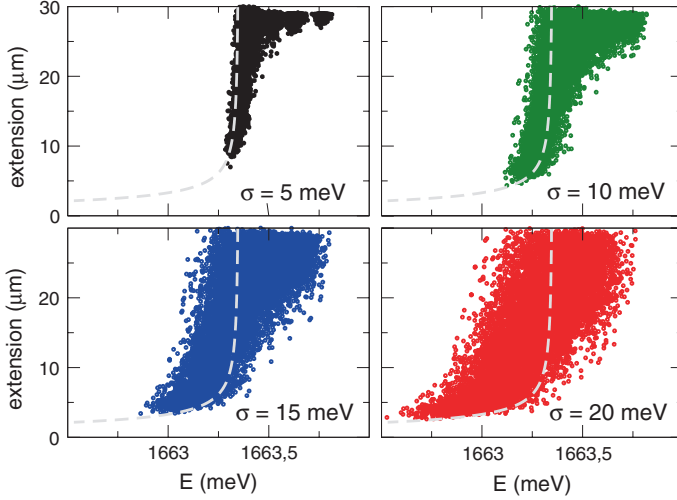


Fig. 2.5 Analysis of real space extension of the lowest four eigenstates of a system similar to that in Fig. 2.4, for 1,000 disorder configurations. Different panels represent results obtained with different value of energetic on-site disorder $\sigma = 5, 10, 15$ and 20 meV. A dashed line, shown in each panels, represents the mean extension of the bound state eigenenergy obtained with the analytical model in (2.10) of a MC with a single excitonic defect, for a LP effective mass $m = 0.5 \times 10^{-5} \text{ meV}$, $R = 100$ nm and varying V_0 from 0 to 50 meV

approximation. We also consider for simplicity a constant excitonic coefficient $C_-^{(\text{ex})}(k) \approx C_-^{(\text{ex})}(0)$ in the restricted k -space near the bottom of the LP branch. In the ICP basis, the Hamiltonian (2.5) is diagonal and, in effective mass approximation, the model Hamiltonian in real space becomes

$$H_{\text{model}} = E_-(0) + \frac{\hbar^2}{2m} \frac{d^2}{dx^2} - V_0 R \delta(x), \quad (2.10)$$

with the effective defect energy $V_0 = \sigma |C_-^{(\text{ex})}(0)|^2$ and effective LP branch mass m . Equation (2.10) allows for a bound level of eigenenergy

$$E_b = E_-(0) - \frac{m V_0^2 R^2}{2 \hbar^2}, \quad (2.11)$$

corresponding to an eigenfunction of the form $\psi(x) = \sqrt{\chi} e^{-\chi|x|}$ of mean extension

$$\lambda_b = \frac{1}{\sqrt{2\chi}} = \frac{\hbar}{2\sqrt{mE_b}}, \quad (2.12)$$

In each panel of Fig. 2.5, we plot λ_b against E_b , while V_0 is varying from 0 to 50 meV. We see that, although taking in account only one excitonic energy defect, the analytical model captures the qualitative behavior of the mean extension

with increasing disorder obtained from the numerical analysis. With diminishing energy, we can see an initial rapid decrease of the localization length (because the LP bottom has relatively flat dispersion curve), after a certain degree of localization, the Fourier components needed in order to further localize the wave function become higher in energy, therefore a further decrease of the localization length requires larger excitonic defects.

As a conclusion of this section, disorder in organic MCs leads to the coexistence of delocalized polariton states with localized ones, distributed in different spectral regions. Localization of strongly coupled states is expected at the LP bottom and near the bare exciton energy. From these two kind of polaritons, completely different behaviors also from the point of view of their time evolutions properties have been predicted [31, 32], with delocalized polaritons featuring a ballistic motion and localized polaritons being instead diffusive.

2.2.2 Relaxation Dynamics

A complete microscopical analysis of the excitation dynamics of a strongly coupled MC should ideally start from a model describing the bare optically active material, and as a second step, this model should be refined for the strong-coupling limit. However, this procedure is difficult in organic MCs where, often, models describing the excitation dynamics in the bare materials are not known or very complex, or do not have a broad range of validity, even in the same class of materials. For this reason, the model developed for describing the full excitation dynamics of J-aggregate MCs in linear regimes [25, 34], which is directly derived as an extension of the Frenkel exciton model of the uncoupled material, assumes also a conceptual importance. This is made possible by the simple description of the bare J-aggregate film as an ensemble of one-dimensional Frenkel exciton systems [23, 35–37] and recurring to a phenomenological ansatz for the polariton wave function [25].

A linear J-aggregate can be considered as a chain composed of N_d monomers (dye molecules) described by the following Frenkel exciton Hamiltonian [23, 35]

$$H = \sum_i^{N_d} E_i b_i^\dagger b_i + \sum_{i \neq j}^{N_d} V_{i,j} (b_i^\dagger b_j + b_j^\dagger b_i) \quad (2.13)$$

The b_i is the monomer exciton operator, and $E_i = \varepsilon_i + D_i^{agg}$ is the sum of the bare energy of the monomer excited state and energy shift due to the interaction of the i th excited molecule with the other molecules and the host medium in their ground states. The exciton transfer term is given by $V_{i,j} = -J/|i - j|^3$, where $J > 0$ is the nearest neighbor coupling strength. When the molecules are put together, the interactions among them give rise to excitation transfer with the formation of delocalized Frenkel excitons (having a 1D energy dispersion curve called J-band) and

thus to the superradiance phenomena. On the other hand, the presence of diagonal disorder is introduced as a Gaussian stochastic fluctuation of the monomer energies; it brings about the fragmentation of the excitons in localized structures on the aggregate chain, especially in the spectral region at the bottom of J-band, with the consequence of inhomogeneous broadening. The diagonal disorder standard deviation is $\sigma = \tilde{\sigma}J$, where $\tilde{\sigma}$ is used as a parameter of the disorder strength. The eigenstates are found by direct diagonalization of the Frenkel exciton Hamiltonian and are described by the following operators:

$$B_{\alpha}^{\dagger} = \sum_i c_i^{(\alpha)} b_i^{\dagger} \quad (2.14)$$

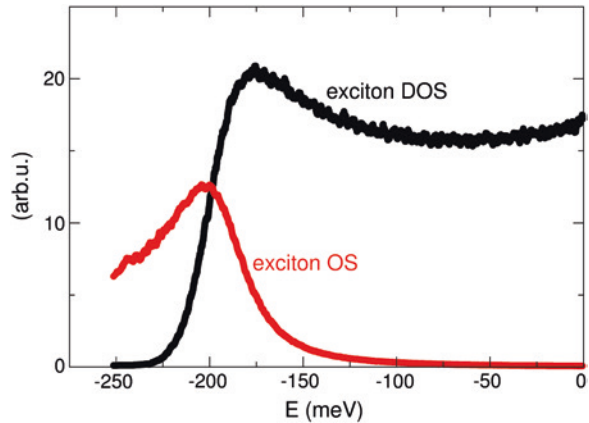
where c_i^{α} is the coefficient of the α th exciton on the i th molecule. The OS of each state is proportional to:

$$F_{\alpha} = \left| \sum_i c_i^{(\alpha)} \right|^2 \quad (2.15)$$

with $\sum_{\alpha} F_{\alpha} = N_d$, with the molecules of equal dipole transition, and with wavelength much greater than the aggregate dimension. In Fig. 2.6, we show the DOS and the OS for state for an ensemble of aggregates with disorder parameter $\tilde{\sigma} = 0.54$ and $J = 75$ meV, averaged over specific spectral intervals. Almost the whole OS of the film is concentrated among the superradiant excitons in a spectral region at the bottom of the J-band.

The Frenkel exciton model for the J-aggregates is then put into contact with a thermal bath that provides a mean for the thermalization of excitations [35–37]. The linear exciton–vibration coupling, treated with the Fermi golden rule, leads to the definition of scattering rates between initial and final excitonic states mediated by the emission/absorption of a vibrational quantum. For a continuous spectrum of vibrations, scattering rates have the following form [35–37]

Fig. 2.6 The DOS of the J-band dispersion (black) for an ensemble of J-aggregate with $\tilde{\sigma} = 0.54$ and the corresponding oscillator strength (red). The oscillator strength (OS) is accumulated in the states at the bottom of the J-band and inhomogeneously broadened by static disorder



$$W_{i',i} = W_0 \Xi_{i,i'} \times (N_{|\Delta E|} + \Theta_{(\Delta E)}) \left(\frac{|\Delta E|}{J} \right)^p, \quad (2.16)$$

while for discrete optical vibrations we obtain

$$W_{i',i} = \frac{2\pi E_{vib}^2}{\hbar} \Xi_{i,i'} \times (N_{|\Delta E|} + \Theta_{(\Delta E)}) \delta(|\Delta E| - E_{vib}), \quad (2.17)$$

where $i = (I, \alpha)$, with I running on different aggregates in the film and α on different Frenkel excitons of the same aggregate, $\Delta E = E_{\alpha'} - E_{\alpha}$, Θ is the step function, N_E is the Bose-Einstein occupation factor of the states of the vibrational bath, $W_0 = 2\pi \xi J / \hbar$, with ξ and p are parameters that describe the strength and spectral shape of the exciton scattering with vibrations [36, 37]. The overlap factor $\Xi_{i,i'}$ is defined as

$$\Xi_{i,i'} = \delta_{I,I'} \sum_{n=1}^{N_d} \left| c_i^{(\alpha)} c_i^{(\alpha')} \right|^2. \quad (2.18)$$

The homogeneous linewidth of the states is due to the radiative lifetime and to the temperature-dependent dephasing processes that are dominated by the exciton-phonon scattering [37]. Each exciton state is broadened as a Lorentzian lineshape around the bare energy E_{α} :

$$g_{\alpha}(E) = \frac{\Delta E_{\alpha} / \pi}{(E_{\alpha} - E)^2 + (\Delta E_{\alpha})^2} \quad (2.19)$$

with the energy uncertainty given by

$$\Delta E_{\alpha} = \hbar \left(\sum_{\alpha'} W_{\alpha',\alpha} + \gamma_{\alpha} \right) \quad (2.20)$$

We can now describe the excitation dynamics of a J-aggregate film, through the definition of rate equations for the Frenkel excitons in the low excitation density approximation

$$\dot{n}_{\alpha} = \sum_{\alpha'} (W_{\alpha,\alpha'} n_{\alpha'} - W_{\alpha',\alpha} n_{\alpha}) - \gamma_{\alpha} n_{\alpha} + P_{\alpha} \quad (2.21)$$

where we have added the radiative decay rate γ_{α} which, for excitons, is given by $\gamma_{\alpha} = F_{\alpha} \gamma_0$, where γ_0 is the spontaneous emission of the dye monomer, typically 0.3 ns^{-1} . We also add a pump term P_{α} on the upper energy tail of the exciton DOS.

This model can be extended to a strongly coupled J-aggregate MC through the introduction of a model polariton wave function, for which we formulate the following ansatz

$$p_{k,\pm}^+ = C_{\pm}^{(ph)}(k) c_k^+ + \frac{C_{\pm}^{(ex)}(k)}{\sqrt{N_{agg}}} \sum_I \sum_{\alpha}^{N_d} \phi_{\alpha,I}^{(k)} B_{\alpha,I}^+ \quad (2.22)$$

where $C_k^{(ex)}$, $C_k^{(ph)}$ are given by (2.8) and $|\phi_{\alpha,I}^{(k)}| = \sqrt{F_\alpha/N_d}$. This allows us to calculate the coupling of polariton states with the thermal bath acting on the molecular Frenkel excitons of the aggregates and to derive the form of the scattering rates between all states of the system [25, 34, 38]. The scattering rates have the same form as (2.16) and (2.17), where now i, i' runs on the excitonic states of the film $n' = (\alpha, I)$, i.e., the α th exciton of the I th aggregate, and on the delocalized polaritons $k = (\pm, q)$, \pm polariton branch and momentum q . However, different overlap factors $\mathcal{E}_{i,i'}$ have to be employed for different processes (we refer to the original literature for the full details [25]). We only mention that overlap factors involving polaritons ($\mathcal{E}_{k,n'}$, $\mathcal{E}_{n',k}$, and $\mathcal{E}_{k',k}$), are suppressed by a factor N_{agg} , being the number of sites on which the polariton state is delocalized. This is due to the contrast between extended polariton states and the localized nature of vibrations.

In addition to the phonon-mediated scattering, we have also considered a radiative pumping rate from exciton to polariton [25, 38] in the following form:

$$W_{\mathbf{k},\alpha}^{\text{rad}} = \beta^{\text{rad}} \gamma_\alpha \frac{|C_k^{(ph)}|^2 g_\alpha(E_k)}{\sum_{\mathbf{k}'} |C_{k'}^{(ph)}|^2 g_\alpha(E_{k'})}. \quad (2.23)$$

Such radiative scattering is proportional to the exciton OS and the transfer matches energy conservation, while the normalization is chosen to obtain a net exciton radiative decay toward polaritons of β^{rad} times the spontaneous emission (γ_α). The broadening g_α is given by (2.19), calculated for the cavity system. This process usually accounts for the presence of a residual weakly coupled excitons in the system, but can also more generally describe the presence of emitting weakly coupled excitons of different nature as it happens in [39], where the authors have engineered a MC with an exciton reservoir (ER) of weakly coupled molecules (chemically different from the molecules giving the strong coupling) resonant with the LP branch bottom. The radiative process described by (2.23) is exploited to efficiently populate of the LP bottom from this ER (which is non-resonantly pumped).

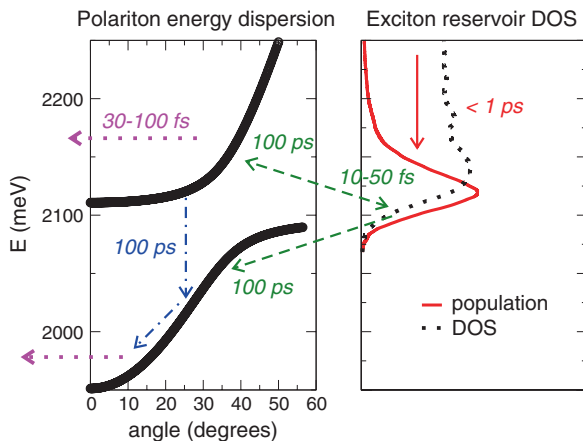
To deal with the 2D MC, we assume isotropic conditions in which the polariton population depends only on the modulus of the wave vector. We describe the dynamics of excitation relaxation by means of a rate equation for the population of state $f_i(t)$:

$$\dot{f}_i(t) = -\Gamma_i f_i(t) + \sum_{i'} (W_{i,i'} f_{i'}(t) - W_{i',i} f_i(t)) + P_i \quad (2.24)$$

where the indices i, i' run over all the spectrum of excitations and can refer to both polariton (k , upper or lower) or localized excitons (n). The damping rate due to the escape through the cavity mirrors is given by $\Gamma_k = |C_\pm^{(ph)}(q)|^2 / \tau_p$. The typical photon lifetime is about $\tau_p = 35$ fs, corresponding to a photon linewidth of the order of 30 meV. P is the pumping rate that we apply as for the aggregate film to the high energy tail of the J-band. For the details of numerical implementation and solution of (2.24) for a J-aggregate MC with a sensible ensemble average over the J-aggregate disorder configurations, see [25].

A comprehensive study of the behavior of this model as a function of its parameters can be found in the original literature [25, 38, 40], including the analysis of the time-dependent solution of (2.24) [40]. We discuss here the overall physical picture that emerges from this model of J-aggregate MCs under non-resonant pumping, which is schematized in Fig. 2.7. The pumping of high energy Frenkel exciton states of the J-aggregates is followed from a rapid relaxation toward the bottom of the excitonic DOS, on timescales shorter than 1 ps. And here, the excitations are accumulated, due to a bottleneck in the relaxation, so that the bottom of the excitonic DOS can be seen as an ER, from which further relaxation on the polaritonic states takes place. The scattering from the ER toward the polariton branches has typical scattering times on the order of 100 ps and therefore cannot lead to an efficient polariton population, due to the short polariton lifetime. The fate of polariton states is twofold. They can be efficiently scattered back into the ER on timescales of the order of 10–50 fs or they can be radiatively emitted on time scales of 30–100 fs. The first process is mainly effective in depleting higher polariton branches, preventing their radiative emission, while generally does not affect the LP branch bottom. This process is the key feature leading to the efficient ultra-fast transfer mechanism between two different excitonic species, mediated by strong coupling, recently observed in hybrid J-aggregate MCs [41]. The relaxation along the polariton branches is frozen due to its long timescales (≈ 100 ps) with respect to the polariton depletion times. The picture of the photophysics of J-aggregate MCs evinced by the model here presented has been validated through the accurate comparison with experimental PL data [26, 42]. As an example, we present in Fig. 2.8 the comparison between the experimentally measured PL data and the corresponding results of a simulation where the scattering with discrete vibrations, observed in Raman spectroscopy have been accounted for. The model is also compatible with the interpretation of ultra-fast spectroscopy measurements [43] and PL excitation spectroscopy data [44].

Fig. 2.7 Scheme of the relaxation mechanism in J-aggregate MC, accounting for molecular exciton DOS and the delocalized polaritons



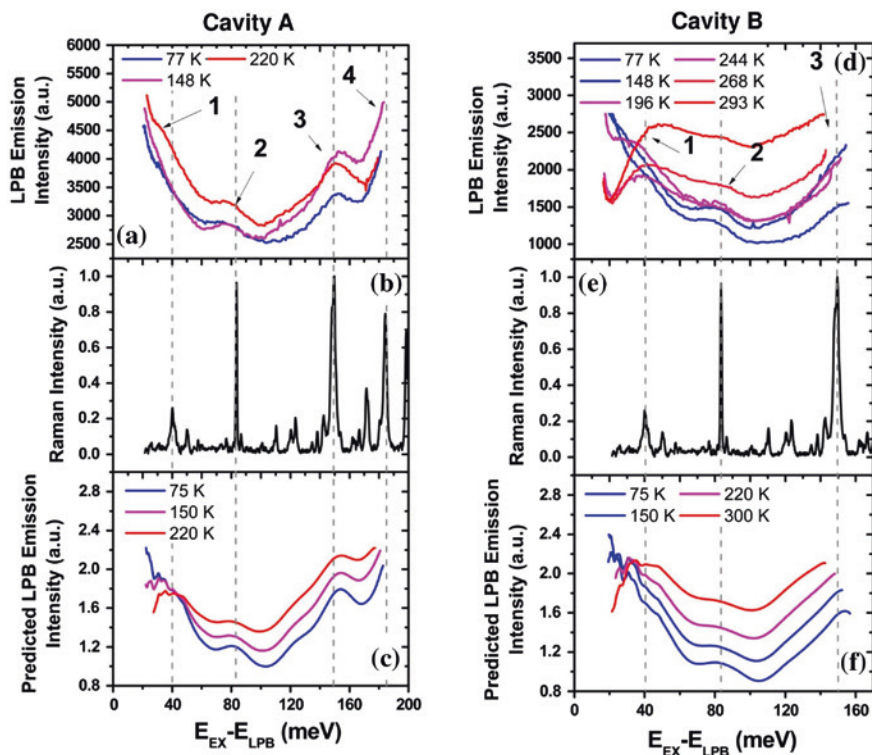


Fig. 2.8 Comparison between the experimental Lambertian-corrected LPB emission intensity as a function of energy separation between the exciton reservoir and the LPB shown in for the cavity A in **a** and for the cavity B in **d**, and the simulated PL emission in **c** and **f** with parameters corresponding to the A and B MCs, respectively. **b** and **e** Raman spectrum of TDBC for the A and B MCs, respectively. Full details on this comparison can be found in [26]. (Reprinted from [26], Copyright 2011, with permission of WILEY-VCH Verlag, Advanced Functional Materials)

2.3 Polariton Lasing in Organic Crystalline Microcavities

Polariton lasing has recently been observed in strongly coupled crystalline anthracene MCs [15], thus providing the first unequivocal experimental proof of nonlinear optics in organic-based MCs. In this section, we focus on some aspects concerning nonlinear physics in such heterostructures.

At high excitation densities, the buildup of a large population at the bottom of the LP branch is favored by bosonic final-state stimulation as soon as the occupation per mode of the LP states exceeds unity. Coherent light-emission, called polariton lasing, results from this macroscopic population due to the finite lifetime of the polaritons which leak out of the cavity via their photonic component. In contrast to the case of inorganic MCs, manifestations of bosonic stimulation using organic cavity polaritons have been quite elusive. Recently, however, several

nonlinear phenomena were reported: Room temperature polariton lasing in an anthracene single crystal MC [15], indirect pumping of J-aggregate lasing MCs [39] (discussed also in Sect. 2.2.2) and even evidence of a polariton condensate featuring a blueshift of the low-energy polariton states [16, 17] (see Fig. 2.9).

In anthracene, the observation of a threshold for nonlinear emission was accompanied by a significant line narrowing and by a collapse of the emission lifetime. In that case, a comparison with the best-case estimate of the threshold for conventional lasing inferred from amplified stimulated emission measurements shows that the lasing threshold observed in the strongly coupled MC is slightly lower than that anticipated for a conventional laser [15]. The temperature dependence of the polariton lasing threshold has also been investigated and shows an order of magnitude decrease from room temperature to low temperatures [45].

Employing two different amorphous organic semiconductors, which also lower the technical intricacies of the fabrication of these samples, two competing groups have been recently able to observe the distinctive features of a polariton condensate once a pumping threshold was overcome [16, 17] (see Fig. 2.9). Measurements recorded with a Michelson interferometer between the emitted light and its retroreflected copy display the appearance of fringes which indicate the phase coherence between different points of the condensate. These important features are accompanied by a blueshift of the emitting polariton, which can be interpreted as the result of the interacting nature of the excitonic part of the polariton. The investigation of the different behaviors of these setups for different temperatures provides distinctive clues of the relaxation mechanisms which characterize these systems.

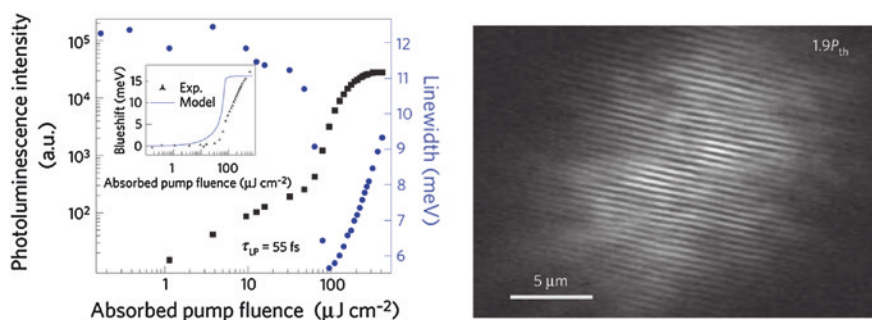


Fig. 2.9 Experimental evidences of polariton condensation in MCs filled with a thin film of 2,7-bis[9,9-di(4-methylphenyl)-fluoren-2-yl]-9,9-di(4-methylphenyl)fluorene. (Left) The dependence of the peak PL intensity (black squares) and linewidth (blue circles) on the absorbed pump fluence is shown for the 120-nm-thick low-Q MC. Note the clear lasing threshold. The inset shows the blueshift of the luminescence peak. (Right) Interferograms recorded in a Michelson interferometer in the retroreflector configuration for above-threshold pump; the fringes are observed over the entire area signal macroscopic phase coherence throughout the condensate. (Reprinted from [17]. Copyright 2014, with permission from Macmillan Publishers Ltd: Nature Materials. Similar measurements are reported in [16])

These remarkable experiments are triggering new theoretical work. In [46], the authors investigate the condensation physics of polaritons where the matter excitations are vibrationally dressed, a typical situation in organic materials. Using mean-field methods, the authors argue on the appearance of sequences of normal-superradiant-normal phases as temperature is decreased. Moreover, for sufficiently strong vibrational couplings, the phase transition can become first order.

The possibility of observing nonlinear phenomena in MCs embedding organic amorphous solids, whose fabrication is easier with respect to inorganic and organic crystals, will surely trigger a boost in the field of polaritonics. Among the several fields where we expect important developments in the next future, we mention here the long-standing goal of realizing an electrically pumped organic laser: The possibility of overcoming the encountered difficulties via the strong-coupling physics is currently renewing the race [47].

In this section, we focus on the lasing measurements in anthracene MCs and present a simple model which describes the onset of the lasing threshold based on a master equation. The mechanism governing the buildup of the polariton population—namely bosonic-stimulated scattering from the ER via a vibronically assisted process—is characterized and its efficiency calculated on the basis of a microscopic theory [48–50].

2.3.1 Two-level Model for Polariton Lasing

In this section, we model the dynamics of the lasing process using a minimal rate-equation approach; we obtain an estimate for the typical timescale of the mechanism which selectively transfers excitations from the reservoir to the bottom of the polariton branch, without any assumptions on its microscopic nature.

2.3.1.1 The Master Equation

The anthracene crystal has two molecules per unit cell and strongly anisotropic optical properties [14, 51]. Excitations in this material are well described within the Frenkel exciton framework, which is based on the intramolecular promotion of an electron from the highest occupied molecular orbital to the lowest unoccupied one. Because of molecular dipole–dipole interaction, the excitation can propagate, resulting in two orthogonal transition dipole moments, $\mu_{a,b}$, directed along the in-plane **a** and **b** axes. When a thin anthracene crystal is placed between two mirrors, light couples to both *a*- and *b*-polarized excitons and creates two orthogonally polarized LP branches. Measurements are usually reported for light polarized along **a** and **b** [15, 51]: In these cases, the *p* and *s* in-cavity light polarizations separately couple to the dipole moments $\mu_{a,b}$ and no mixing effect is present.

We focus only on *b*-polarized excitons [14], i.e., those with largest OS, for which lasing has been reported [15] and neglect other polaritonic and excitonic states. The initial relaxation of the pump excitations is also neglected, and the presence of an effective excitonic reservoir at a fixed energy independent on the cavity properties is considered [25]. We note that the experimental PL from anthracene MCs shows always a clear maximum at energy ~ 2.94 eV regardless of the cavity thickness [15, 52], and indeed lasing has been achieved in a cavity where the minimum of the LP is exactly at 2.95 eV. This is a signature that the microscopic dynamics resulting in the lasing phenomenon is that of a two-level process rather than that of the well-known polariton bottleneck. We thus develop a two-level master equation for $v_e(t)$ and $v_p(t)$, the surface density of reservoir excitons and of lasing polaritons located near $\mathbf{k} = 0$, respectively.

We denote with \mathcal{A}_0 the subregion of the Brillouin zone located around $\mathbf{k} = 0$ which is occupied by the lasing polaritons. Because states at the bottom of the LP branch do not have a well-defined wave vector k , we consider all of the localized wave packets with energy $\sim E_{LP}(\mathbf{k} = 0)$ as equally contributing to the lasing process. N_{pol} is the number of such polaritonic states, while N_{exc} is the number of excitonic states. The polariton and exciton decay rates are $\Gamma_p = |C^{(\text{ex})}|^2/\tau_e + |C^{(\text{ph})}|^2/\tau_p$ and $\Gamma_e = 1/\tau_e$, respectively, where $\tau_p(\tau_e)$ is the bare photon (exciton) lifetime and $C^{(\text{ph})}(C^{(\text{ex})})$ is the photonic (excitonic) Hopfield coefficient for the lasing polaritons.

The parameter Z^e is the decay rate via other channels, such as phonons, LPs outside the \mathcal{A}_0 region and leaky modes, whereas bimolecular quenching processes are treated separately, with a rate γ' . A standard pump term proportional to $P'(t)$ is included; in order to take into account possible saturation effects the term $(1 - v_e/\bar{v}_e)$ has been considered ($\bar{v}_e = N_{\text{exc}}/A$ is the surface density of excitonic states and A is the area of the sample).

The rate of resonant excitation transfer from the reservoir to the lasing polaritons is W^{ep} . We retain the bosonic enhancement term $(1 + v_p/\bar{v}_p)$ responsible for lasing effects, where $\bar{v}_p = N_{\text{pol}}/A$ is the surface density of polaritonic states.

The master equation for $v_e(t)$ and $v_p(t)$, whose physics is sketched in Fig. 2.10, reads (see [50] for the full derivation and more comprehensive discussion):

$$\begin{aligned} \dot{v}_e = & -\Gamma_e v_e - W^{\text{ep}} v_e \left(1 + \frac{v_p}{\bar{v}_p}\right) - Z^e v_e - \gamma' v_e \left(v_e + |C^{(\text{ex})}|^2 v_p\right) \\ & + \left(1 - \frac{v_e}{\bar{v}_e}\right) P'(t) \end{aligned} \quad (2.25a)$$

$$\dot{v}_p = -\Gamma_p v_p + W^{\text{ep}} v_e \left(1 + \frac{v_p}{\bar{v}_p}\right) - \gamma' \left(v_e + |C^{(\text{ex})}|^2 v_p\right) |C^{(\text{ex})}|^2 v_p \quad (2.25b)$$

Note that the resulting equations are completely analogous to those describing conventional lasing [53], with the important difference that the lasing state is a polariton and thus retains an excitonic component.

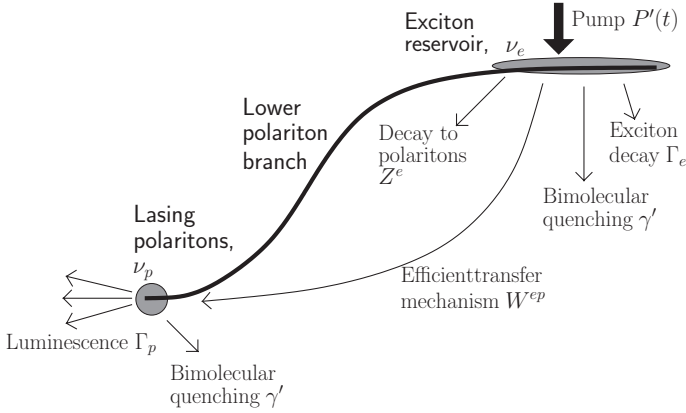


Fig. 2.10 Sketch of the LP branch and of the physical processes and scattering mechanisms included in the master equation (2.1). (Reprinted from [50], Copyright 2013, with permission from American Physical Society)

2.3.1.2 Parameters

We relate (2.25a) and (2.25b) to the experimental system in [15] using the following parameters.

Anthracene Crystal. The experimental MC embeds a crystal of anthracene with thickness $L_z = 120$ nm; the molecular density is $\rho_0 = 4.2 \times 10^{21} \text{cm}^{-3}$. We ignore the monoclinic structure of the unit cell and instead estimate its linear size as $a = (\rho_0/2)^{-1/3} = 7.8 \times 10^{-8} \text{cm}$, including the presence of two molecules per unit cell. The number of layers is estimated as $N = L_z/a \approx 153$. The absorption maximum of the anthracene crystal is at energy $E_0 = 3.17 \text{eV}$. The exciton measured lifetime is of the order of $\tau_e \sim 1 - 3$ ns and in the next simulations, we take the intermediate value $\tau_e = 2$ ns. The contribution of Z^e is neglected because it can be included into τ_e without any substantial difference as long as $\tau_e < 1/Z^e$, which can be safely assumed.

MC and Polaritons. If we assume homogeneous broadening, the cavity lifetime can be estimated from the polariton linewidth at $\mathbf{k} = 0$, where it is mostly photon-like. Using this approach, we obtain a lower bound $\tau_p = 85$ fs. An exact calculation assuming perfect interfaces for the mirrors results in an upper bound $\tau_p = 1$ ps. We will estimate W^{ep} corresponding to both extrema. The Hopfield coefficients of the LP branch are [51]: $C^{(\text{ph})} = 0.92$ and $C^{(\text{ex})} = 0.39$.

For small $|\mathbf{k}|$, the \mathcal{A}_0 region has cylindrical symmetry [54–56]. Its radius, q_0 , can be estimated using $E_{LP}(q_0) - E_{LP}(k=0) = \Gamma_0/2$, where $\Gamma_0 = 15 \text{meV}$ is the linewidth of polaritons at $\mathbf{k} = 0$ below threshold [15]; we obtain $q_0 = 2.2 \times 10^4 \text{cm}^{-1}$.

Pump. The pump density is: $P'(t) = P'_0 \exp[-t^2/(2\sigma_t^2)]$ ($\sigma_t \sim 64$ fs), with $P'_0 = P_0/(\pi r_0^2 \hbar \omega_{\text{pump}})$ where $r_0 = 110 \mu\text{m}$ is the radius of the pump spot and $\hbar \omega_{\text{pump}} = 3.45 \text{eV}$ is the energy of the pump photons. P_0 can be derived from the

relation $E_{\text{tot}} = \int P(t)dt = \sqrt{2\pi}P_0\sigma_t$, where E_{tot} is the experimentally measured total absorbed energy.

Bimolecular Quenching Rate. To the best of our knowledge, there are no measurements of the bimolecular quenching rate, γ' , for 2D anthracene crystals. According to the standard theory for bimolecular quenching [14], $\gamma_{3D} = 8\pi RD$, where R is the Förster radius of the exciton and sets the volume around the exciton in which annihilation happens, while D is the diffusion coefficient of excitons. Measurements for 3D anthracene crystals have yielded values of [14] $\gamma_{3D} = 10^{-8}\text{cm}^3\text{s}^{-1}$ and [14, 57] $D \sim 1 - 10 \times 10^{-3}\text{cm}^2\text{s}^{-1}$. The corresponding diffusion length $\ell = (\tau_e D)^{1/2} \sim 1 - 3 \times 10^{-6}\text{cm}$ is smaller than $L_z = 1.2 \times 10^{-5}$ and suggests that excitons can be treated as diffusing in a 3D environment. As a result, we initially fix $\gamma' = \gamma_{3D}/L_z = 7 \times 10^{-4}\text{cm}^2\text{s}^{-1}$.

2.3.1.3 Results

Since all other parameters are known, we leave only W^{ep} as a fit parameter. We numerically integrate (2.25a) and (2.25b) and once the complete time-dependent functions $v_{e,p}(t)$ are known we compute the integral $\int v_p(\tau)d\tau$ and compare it with the experimental values.

In Fig. 2.11, the fits obtained for the extreme values of $\tau_p = 85\text{ fs}$ and 1 ps are shown. The value of W^{ep} has been fit to the experimentally observed threshold

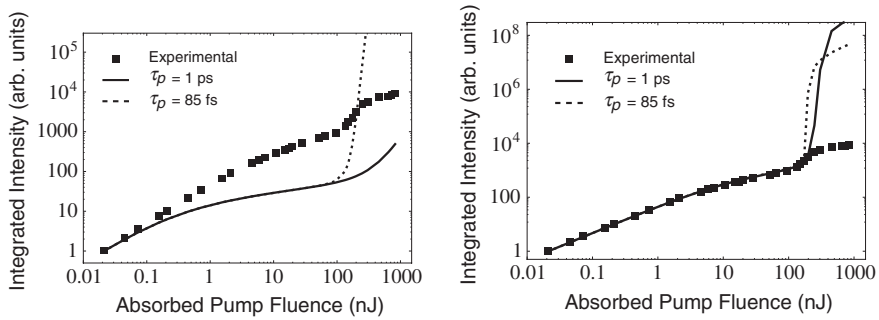


Fig. 2.11 Time-integrated surface density of polaritons $\int v_p(\tau)d\tau$ calculated from solution of (2.25a) and (2.25b) (lines) and from experimental data (squares). The input calculation parameters are: (i) $\tau_p = 85\text{ fs}$ (dashed line) and (ii) $\tau_p = 1\text{ ps}$ (solid line). (Left) The bimolecular quenching rate is taken from the measured 3D bulk value: $\gamma' = \gamma_{3D}/L_z$. (Right) The bimolecular quenching parameter γ' is used to fit the below-threshold behavior of the experimental data. The fit yields the following values for W^{ep} : $7 \times 10^5\text{ s}^{-1}$ and $7 \times 10^5\text{ s}^{-1}$, respectively. The fit yields the following values for γ' : $1.5 \times 10^{-5}\text{ cm}^2\text{ s}^{-1}$ and $\gamma' : 1.6 \times 10^{-5}\text{ cm}^2\text{ s}^{-1}$, respectively. Regarding W^{ep} , the results are: $4 \times 10^5\text{ s}^{-1}$ and $3.5 \times 10^4\text{ s}^{-1}$, respectively. Because the experimental data is in arbitrary units, here and in the following fits the experimental data is normalized so that the first experimental and theoretical points coincide. (Reprinted from [50], Copyright 2013, with permission from American Physical Society)

value. In both cases, W^{ep} is of the order 10^5 s^{-1} . The agreement with the experiment is poor and it is apparent that the chosen value of γ' does not properly describe the transition between linear and sublinear region below threshold. Note that the exciton lifetime $\tau_e \sim 2 \text{ ns}$ is shorter than the reported bulk value [14] $\tau_{e,\text{bulk}} \sim 10 \text{ ns}$; surface interactions or defects within the layers could explain this discrepancy. In this situation, the excitonic diffusion coefficient can be smaller, resulting in a reduced possibility for excitons to pairwise annihilate.

Because a fit of γ' which determines the onset of bimolecular quenching can be readily decoupled from that of W^{ep} , both parameters are allowed to vary and the resulting fits are shown in Fig. 2.11. We obtain $\gamma' \approx 1.5 \times 10^{-5} \text{ cm}^2 \text{ s}^{-1}$ independently of τ_p , as expected. Note that this value is two orders of magnitude smaller than γ_{3D}/L_z . The resulting values for W^{ep} are $4 \times 10^5 \text{ s}^{-1}$ and $3.5 \times 10^4 \text{ s}^{-1}$ for $\tau_p = 85 \text{ fs}$ and 1 ps , respectively. Even if the scattering process acts on a sensibly longer timescale compared to the exciton and polariton lifetimes, it can lead to observable effects in presence of high excitonic densities. We can roughly estimate the surface density of excitons at threshold via $\Gamma_p v_p = W^{\text{ep}} v_e (1 + v_p/\bar{v}_p)$. Assuming that at threshold $v_p = \bar{v}_p$, we obtain:

$$\frac{v_{e,\text{th}}}{\bar{v}_e} = \frac{\bar{v}_p}{\bar{v}_e} \frac{\Gamma_p}{2 W^{\text{ep}}} \sim 0.01 \quad (2.26)$$

The density of excitations is thus extremely high, though not unrealistic. Moreover, this is consistent with what shown in Fig. 2.12, where at threshold, the peak exciton value is of few percents. Note that $v_{e,\text{th}}/\bar{v}_e$ does not depend on the value of q_0 , because both W^{ep} and \bar{v}_p depend linearly on the size of the \mathcal{A}_0 region.

Note that even if the two fits yield very different values for W^{ep} , the fit is not ill-conditioned. The fit of the below-threshold region depends only on two parameters, $\tau_p W^{\text{ep}}$ and γ' . It is our ignorance of τ_p , whose value can vary by more than one order of magnitude and still be compatible with the measurements, which propagates an uncertainty of one order of magnitude on W^{ep} . In Sect. 2.3.2, we show a simple analytical model which corroborates this picture.

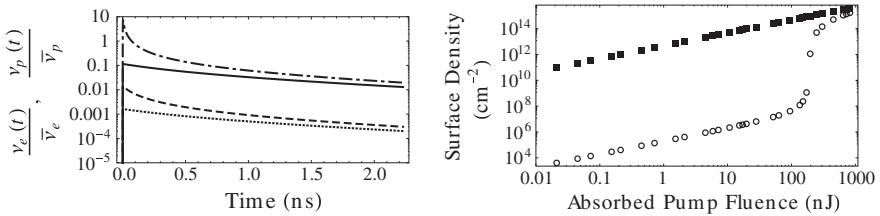


Fig. 2.12 (Left) Time dependence of the normalized surface density of excitons $v_e(t)/\bar{v}_e$ and of polaritons $v_p(t)/\bar{v}_p$ below threshold (≈ 0.047 , dotted line and solid line, respectively) and at threshold ($E_{\text{tot}} = 150 \text{ nJ}$, dashed line and dashed-dotted line) plotted for $\tau_p = 85 \text{ fs}$. Note that this time dependence is in good agreement with that reported in [15]. (Right) Maximal population density of excitons $\max_t v_e(t)$ (squares) and of lasing photons $\max_t v_p(t)$ (circles). See Fig. 2.11 for the parameters; $\tau_p = 85 \text{ fs}$ (Reprinted from [50], Copyright 2013, with permission from American Physical Society)

Although the fit below threshold is excellent, the region above threshold is poorly described. It can be seen in Fig. 2.12, which shows the time dependence and peak of the normalized surface exciton and polariton densities, that at threshold, the exciton density reaches a few percent of the total molecular density. Such high excitation densities may require a more refined description of the annihilation process. Indeed, our calculation above threshold seems to be in better agreement with recent low-temperature data, where the threshold occurs at lower excitation density [45]. Moreover, above threshold, when the polariton density becomes important, the details of the theoretical model used for the polariton–polariton bimolecular quenching become important [58–60]. Note that the mean-field polariton–polariton interaction [61] has not been included.

2.3.2 Analytical Model Below Threshold

We present an analytical solution of (2.25a) and (2.25b) for the pump regime below threshold. For simplicity, we assume that the pumping process happens at a timescale faster than the polariton dynamics, so that at time $t = 0$, there is an exciton density:

$$v_e(t = 0) = \int_0^\infty P'(\tau) d\tau \doteq v_{e0}. \quad (2.27)$$

We thus consider the following master equation:

$$\dot{v}_e = -\Gamma_e v_e - W^{ep} v_e - Z^e v_e - \gamma' v_e v_e; \quad v_e(t = 0) = v_{e0}; \quad (2.28a)$$

$$\dot{v}_p = -\Gamma_p v_p + W^{ep} v_e; \quad v_p(t = 0) = 0. \quad (2.28b)$$

Because the density of polaritons is much smaller than the density of excitons we can exclude the polariton contribution to bimolecular quenching. Moreover, the whole bimolecular quenching in (2.28b) has been neglected because $\Gamma_p \gg \gamma' |C^{(ex)}|^2 v_e(t) \forall t$. Indeed, for it to be relevant, the 2D density of reservoir excitons should be larger than $\Gamma_p / (\gamma' |C^{(ex)}|^2) \sim 4 \times 10^{17} \text{cm}^{-2}$, which is unrealistic (see for example Fig. 2.12).

The solution of (2.28a) is:

$$v_e(t) = v_{e0} e^{-(\Gamma_e + W^{ep} + Z^e)t} \left[1 + \gamma' v_{e0} \frac{1 - e^{-(\Gamma_e + W^{ep} + Z^e)t}}{\Gamma_e + W^{ep} + Z^e} \right]^{-1}. \quad (2.29)$$

The integrated polariton PL, which is fitted in Fig. 2.11, is:

$$\int_0^\infty v_p(\tau) d\tau = -\frac{v_p(\tau)}{\Gamma_p} \Big|_0^\infty + \frac{W^{ep}}{\Gamma_p} \int_0^\infty v_e(\tau) d\tau = \frac{W^{ep}}{\Gamma_p \gamma'} \log \left[1 + \frac{\gamma' v_{e0}}{\Gamma_e + W^{ep} + Z^e} \right]$$

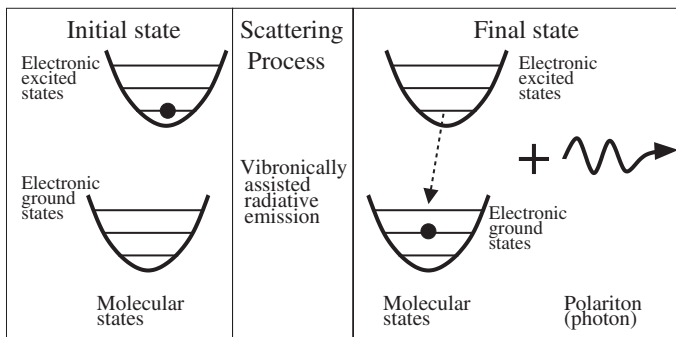


Fig. 2.13 Sketch of the radiative microscopic mechanism responsible for the efficient excitation transfer in the Franck–Condon approximation. (Reprinted from [50], Copyright 2013, with permission from American Physical Society)

Let us now observe that in our system $\Gamma_e \gg W^{\text{ep}}, Z^e$ and that the experimental data are proportional to $\int \nu_p d\tau$ via an unknown constant, which in the fits in Sect. 2.3.1 is chosen so that the experimental and theoretical points for the lowest pump fluence coincide. This makes the fit of the below-threshold region dependent only on γ' and independent on W^{ep} and τ_p .

2.3.3 The Scattering Mechanism

In this section, we focus on the microscopic origin of the excitation transfer of Sect. 2.3.1 and propose as the relevant scattering mechanism the radiative recombination of a molecular exciton assisted by the emission of a vibrational quantum of the electronic ground state. We show that the resulting scattering rate is in good agreement with that obtained in the previous section; we also consider an alternative and possibly coexisting model based on the non-radiative emission of an optical phonon [62].

2.3.3.1 Radiative Transition

The absorption and PL spectra of anthracene show several vibronic resonances [63]. The resonances observed in absorption correspond to the molecular vibrations of the first electronically excited state, and those in PL to the vibrations of the electronic ground state [14]. Strong light-matter coupling has only been demonstrated for the former [64], since the fraction of vibrationally excited ground-state molecules is negligible at room temperature. However, as shown schematically in Fig. 2.13, the transitions responsible for the vibronic structure in PL result in the scattering of excitons to lower energy polaritons, where

the missing energy exactly corresponds to that of the vibrational quantum, $E_{01} \sim 173$ meV [49]. In [50] we discuss the approximations needed to apply the known microscopic theory [49, 55] to the present system [51] and refer to such reference for a more comprehensive analysis, whose main ideas are here only sketched.

We develop a microscopic expression for the scattering rate W^{jk} from one molecular exciton (labeled by j) to a lasing polariton (labeled by k) which involves the parameters of an anthracene MC [50]:

$$W^{jk} \approx \frac{V_1^2}{\hbar} \frac{\pi^2 S |C^{(\text{ph})}|^2}{2} \frac{1}{MN} \delta(E_0 - E_{\text{LP}}(\mathbf{k}) - E_{01}) \quad (2.30)$$

V_1 is the strength of the light-matter coupling as extracted from a simple coupled-harmonic-oscillators model [51]; S is the Huang-Rhys parameter, which is approximately ~ 1 [65]. M is the number of unit cells in the 2D quantization surface and N is the number of anthracene monolayers. E_0 is the energy of the ER, E_{01} the energy of the vibronic quantum, and $E_{\text{LP}}(\mathbf{k})$ the dispersion relation of the LP branch.

Working in the energy space and defining the spectral region of lasing polaritons $E \in [E_{\text{inf}}^{\mathcal{A}_0}, E_{\text{sup}}^{\mathcal{A}_0}]$ and the polariton DOS $D(E)$, we get:

$$W^{ep} = \int_{E_{\text{inf}}^{\mathcal{A}_0}}^{E_{\text{sup}}^{\mathcal{A}_0}} \frac{V_{1\pm}^2}{\hbar} \frac{\pi^2 S |C^{(\text{ph})}|^2}{2MN} f(E_0 - E - E_{01}) D(E) dE; \quad (2.31)$$

where the delta function $\delta(E)$ has been substituted by the normalized lineshape of the (0-1) PL, dubbed here $f(E)$. The 2D density of state is

$$D(E) = \frac{mMa^2}{2\pi\hbar^2} \theta[E - E_{\text{LP}}(\mathbf{k} = 0)],$$

where the effective mass m can be obtained from the fits of the dispersion relations: $m \sim 1.7 \times 10^{-5} m_e$; moreover $\bar{v}_e = 2N/a^2$. The normalized linewidth of (0-1) PL $f(E)$ is a Lorentzian centered in zero with FWHM $\Gamma = 100$ meV; we also assume $E_{\text{inf}}^{\mathcal{A}_0} = E_0 - E_{01} = E_{\text{LP}}(\mathbf{k} = 0)$, whereas $E_{\text{sup}}^{\mathcal{A}_0} = E_{\text{inf}}^{\mathcal{A}_0} + 7.5$ meV (see Sect. 2.3.1). We obtain:

$$W^{ep} = \frac{\pi S |C^{(\text{ph})}|^2}{2} \frac{mV_1^2}{\bar{v}_e \hbar^3} \int_{E_{\text{inf}}^{\mathcal{A}_0}}^{E_{\text{sup}}^{\mathcal{A}_0}} f(E_{\text{inf}}^{\mathcal{A}_0} - E) dE. \quad (2.32)$$

The rate before the integral is equal to $\approx 1.0 \times 10^7 \text{s}^{-1}$, while the contribution from the integral, which comes from the lineshape, is ≈ 0.047 . Thus, the theoretical microscopic mechanism is $W^{ep} \approx 5 \times 10^5 \text{s}^{-1}$.

Because the theoretical model neglects effects which can possibly lower the efficiency of the resonant scattering, we consider our estimate to be in good agreement with the values estimated from data in Sect. 2.3.1.

2.3.3.2 Non-radiative Transition

We now consider an alternative and possibly coexisting relaxation channel, which is non-radiative [62]. An exciton is scattered from the reservoir to one polariton state by the emission of a molecular vibration of the electronic excited state. This is due to the intramolecular exciton–phonon coupling [4, 66] which has been demonstrated to play a key role in the modeling of the PL of J-aggregates MCs [26, 38] (see also Sect. 2.2.2).

Note that in this case, the considered phonon belongs to the electronic excited state, whereas in the radiative case, it was related to the electronic ground state. Moreover, the resulting scattering element W^{ek} includes the excitonic content of the out coming polariton, whereas (2.32) is weighted by the photonic Hopfield coefficient. The scattering rate from one molecular exciton (labeled by j) to one lasing polariton (labeled by k) is given by [62]:

$$W^{jk} = \frac{2\pi}{\hbar} SE_{11}^2 \frac{|C^{(e)}|^2}{2NM} \delta(E_0 - E_{LP}(\mathbf{k}) - E_{11}) \quad (2.33)$$

where $\sqrt{S} \sim 1$ is the strength of the exciton–phonon coupling [65] and E_{11} is the energy quantum of a vibration of the excited state. Even if the Franck–Condon model which we are using prescribes $E_{11} = E_{01}$, this is not necessarily true in general. The factor $|C^{(ex)}|^2/(2NM)$ is the Hopfield coefficient for the exciton of the molecule j relative to the polariton k [62].

The comparison of (2.33) with (2.30) for the radiative case shows that the ratio of the two processes is:

$$\frac{W_{\text{RAD}}^{jk}}{W_{\text{NON-RAD}}^{jk}} = \frac{\pi V_1^2}{2E_{11}^2} \cdot \frac{|C^{(\text{ph})}|^2}{|C^{(\text{ex})}|^2}. \quad (2.34)$$

Since both V_1 and E_{11} are of the same order of magnitude, 100 meV, the efficiency ratio mainly depends on the Hopfield coefficients of the bottom polaritons. Thus, as in our case $|C^{(\text{ph})}|^2/|C^{(\text{ex})}|^2 \approx 5$, we expect the radiative mechanism to be the main origin of the excitation transfer which results in lasing, even if to understand the importance of the non-radiative transfer a more detailed analysis is necessary. An experimental analysis exploring several organic crystals would thus be of the greatest interest.

2.3.4 The Effect of Temperature

Reported data for anthracene MCs show a reduction of the lasing threshold of slightly less than an order of magnitude once temperature is lowered from 300 to

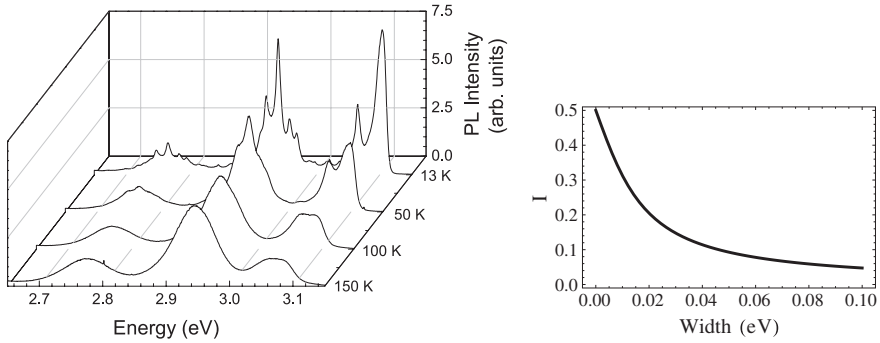


Fig. 2.14 (Left) PL spectra of anthracene layers for temperatures between 13 and 150 K (courtesy of S. Kéna-Cohen). (Right) Dependence of the integral (35) appearing in (32) on the width of $f(E)$, which is a Lorentzian function

12 K [45]. In this section, we discuss temperature effects within the framework of the developed model and the related consequences on the lasing properties.

Experimental studies on the PL from bulk anthracene crystals have shown a strong temperature dependence characterized by considerable spectral narrowing [67]. The temperature dependence obtained using thin crystals grown from solution is shown in Fig. 2.14. Here, the crystals were grown on silicon substrates to ensure good thermal contact to the cryostat cold finger and were excited using 1 ns-long pulses at $\lambda = 337$ nm. A composite vibronic structure emerges, which can be understood in terms of a high-energy phonon (considered in this work) and of a low-energy phonon, which is not resolved at room temperature because of thermal broadening. Such a system requires the use of two-phonon states in order to exactly reproduce the spectra [68]; however, we ignore this complication because we are only interested in the phenomenological properties of the line which is responsible for lasing.

The scattering rate W^{ep} in (2.32) depends on temperature via $f(E)$. On the one hand, at low temperature, the Lorentzian is narrower, and thus a smaller fraction of the OS is dispersed into non-lasing modes. On the other hand, only a fraction of the OS of the (0–1) transition contributes to lasing, because the other lines are far detuned. Additionally, both the quantum yield, estimated at room temperature to be 0.5, and the exciton lifetime τ_e are expected to increase at low temperature.

In Fig. 2.14, we compute the dependence of the integral appearing in (2.32):

$$I \doteq \int_{E_{\text{inf}}^{\mathcal{A}_0}}^{E_{\text{sup}}^{\mathcal{A}_0}} f(E_{\text{inf}}^{\mathcal{A}_0} - E) \, dE \quad (2.35)$$

on the width of the Lorentzian function $f(E)$ which represents the normalized spectrum of the (0–1) PL emission. Whereas at room temperature, the FWHM is ≈ 0.1 eV, at 12 K, it is $\sim 0.01 - 0.02$ eV, and thus W^{ep} increases of at least a factor of 5.

Roughly speaking, the observed thermal reduction of the threshold is of less than one order of magnitude [45], and thus similar to the numbers of our estimates. This points out a possible connection between the temperature dependence of the laser threshold and of the PL of anthracene crystals. A more systematic analysis, both theoretical and experimental, goes beyond the scope of this work and will be the focus of future investigations. As long as the thermal linewidth narrowing is considered, we observe that when the radiative transition is not perfectly resonant with the lasing, it could even result in the opposite effect.

For the sake of completeness, in [50], we also include the thermal population of the vibrations of the molecular ground state in the master (2.25a) and demonstrate that it can be safely neglected.

Concluding, we have presented a minimal model to describe the polariton lasing physics observed in crystalline anthracene MCs. Only the essential features of the physical processes involved have been included: The incoherently pumped ER, the vibronically assisted radiative scattering from the reservoir to the bottom of the LP branch, the onset of bosonic stimulation and the buildup of the polariton population with increasing pump intensity, the polariton losses through the mirrors, and bimolecular quenching processes. All the relevant material parameters, except from the bimolecular quenching rate, have been determined independently from the experimental data on the pump dependence of the polariton emission. In particular, the efficiency of the scattering mechanism here considered—which takes into account the prominent role of vibronic replicas in the photophysics of anthracene MCs—has been calculated microscopically. The numerical simulations obtained are in good agreement with the data and describe well the onset of the nonlinear threshold for polariton lasing.

Acknowledgements We would like to thank for many insightful discussions V.M. Agranovich, S. Kéna-Cohen, D. Lidzey, R. Mahrt, L. Silvestri. We acknowledge financial support from the European FP7 ICARUS program (Grant Agreement No. 237900), the Regione Toscana POR FSE 2007-2013, and the Deutsche Forschungsgemeinschaft.

References

1. M.S. Skolnick, T.A. Fisher, D.M. Whittaker, *Semicond. Sci. Technol.* **13**, 645 (1998)
2. A. Kavokin, J.J. Baumberg, G. Malpuech, F.P. Laussy, *Microcavities* (Oxford University Press, Oxford, 2007)
3. I. Carusotto, C. Ciuti, *Rev. Mod. Phys.* **85**, 299 (2013)
4. V.M. Agranovich, *Excitations in Organic Solids* (Oxford University Press, Oxford, 2009)
5. F. Bassani, G.P. Parravicini, *Electronic States and Optical Transitions in Solids* (Pergamon Press, Oxford, 1975)
6. M. Born, K. Huang, *Dynamical Theory of Crystal Lattices* (Oxford University Press, Oxford, 1954)
7. C. Weisbuch, M. Nishioka, A. Ishikawa, Y. Arakawa, *Phys. Rev. Lett.* **69**, 3314 (1992)
8. J. Kasprzak, M. Richard, S. Kundermann, A. Baas, P. Jeambrun, J.M.J. Keeling, F.M. Marchetti, M.H. Szymańska, R. André, J.L. Staehli, V. Savona, P.B. Littlewood, B. Deveaud, L.S. Dang, *Nature* **443**, 409 (2006)

9. V.M. Agranovich, H. Benisty, C. Weisbuch, Solid State Commun. **102**, 631 (1997)
10. D.G. Lidzey, D.D.C. Bradley, M.S. Skolnick, T. Virgili, S. Walker, D.M. Whittaker, Nature (London) **395**, 53 (1998)
11. R.F. Oulton, N. Takada, J. Koe, P.N. Stavrinou, D.C.C. Bradley, Semicond. Sci. Technol. **18**, S419 (2003)
12. D.G. Lidzey, in *Electronic Excitations in Organic Based Nanostructures*, ed. by V.M. Agranovich, F. Bassani (Elsevier, Amsterdam, 2003), p. 355
13. V.M. Agranovich, Y.N. Gartstein, M. Litinskaya, Chem. Rev. **111**, 5179 (2011)
14. M. Pope, C.E. Swenberg, *Electronic Processes in Organic Crystals and Polymers* (Oxford University Press, Oxford, 1999)
15. S. Kéna-Cohen, S. Forrest, Nat. Photonics **4**, 371 (2010)
16. J.D. Plumhof, T. Stoferle, L. Mai, U. Scherf, R.F. Mahrt, Nat. Mater. **13**, 247 (2014)
17. K.S. Daskalakis, S.A. Maier, R. Murray, S. Kéna-Cohen, Nat. Mater. **13**, 272 (2014)
18. R.J. Holmes, S. Kéna-Cohen, V.M. Menon, S.R. Forrest, Phys. Rev. B **74**, 235211 (2006)
19. J. Wenus, R. Parashkov, S. Ceccarelli, A. Brehier, J.S. Lauret, M.S. Skolnick, E. Deleporte, D.G. Lidzey, Phys. Rev. B **74**, 235212 (2006)
20. D.G. Lidzey, D.D.C. Bradley, A. Armitage, M.S. Skolnick, Science **288**, 1620 (2000)
21. P. Schouwink, H.V. Berlepsch, L. Dähne, R.F. Mahrt, Chem. Phys. Lett. **344**, 352 (2001)
22. S. Ceccarelli, J. Wenus, M.S. Skolnick, D.G. Lidzey, Superlattices Microstruct. **41**, 289 (2007)
23. T. Kobayashi (ed.), *J-Aggregates*, (World Scientific, Singapore, 1996)
24. P. Michetti, G.C. La Rocca, Phys. Rev. B **71**, 115320 (2005)
25. P. Michetti, G.C. La Rocca, Phys. Rev. B **77**, 195301 (2008)
26. D.M. Coles, P. Michetti, C. Clark, W.C. Tsoi, A.M. Adawi, J.-S. Kim, D.G. Lidzey, Adv. Func. Mat. **21**, 3691 (2011)
27. M.D. Fayer, in *Spectroscopy and Excitation Dynamics of Condensed Molecular Systems*, ed. by V.M. Agranovich, R.M. Hochstrasser, (North-Holland, NY, 1983) p. 185
28. V.M. Agranovich, M. Litinskaia, D.G. Lidzey, Phys. Rev. B **67**, 85311 (2003)
29. V.M. Agranovich, G.C. La Rocca, Solid State Commun. **135**, 544 (2005)
30. M. Litinskaya, P. Reineker, Phys. Rev. B **74**, 165320 (2006)
31. V.M. Agranovich, Y.N. Gartstein, Phys. Rev. B **75**, 75302 (2007)
32. P. Michetti, G.C. La Rocca, Physica E **40**, 1926 (2008)
33. D.G. Lidzey, D.D.C. Bradley, T. Virgili, A. Armitage, M.S. Skolnick, S. Walker, Phys. Rev. Lett. **82**, 3316 (1999)
34. P. Michetti, G.C. La Rocca, Phys. Status Solidi B **245**, 1055 (2008)
35. M. Bednarz, V.A. Malyshev, J. Knoester, J. Chem. Phys. **117**, 6200 (2002)
36. M. Bednarz, V.A. Malyshev, J. Knoester, Phys. Rev. Lett. **91**, 217401 (2003)
37. D.J. Heijs, V.A. Malyshev, J. Knoester, Phys. Rev. Lett. **95**, 177402 (2005)
38. P. Michetti, G.C. La Rocca, Phys. Rev. B **79**, 035325 (2009)
39. G.M. Akselrod, E.R. Young, M.S. Bradley, V. Bulovic, Opt. Expr. **21**, 12122 (2013)
40. P. Michetti, G.C. La Rocca, Phys. Status Solidi C **6**, 403 (2009)
41. D.M. Coles, N. Somaschi, P. Michetti, C. Clark, P.G. Lagoudakis, P.G. Savvidis, D.G. Lidzey, Nat. Mater. (2014). doi:[10.1038/nmat3950](https://doi.org/10.1038/nmat3950)
42. D.M. Coles, P. Michetti, C. Clark, A.M. Adawi, D.G. Lidzey, Phys. Rev. B **84**, 205214 (2011)
43. T. Virgili, D. Coles, A.M. Adawi, C. Clark, P. Michetti, S.K. Rajendran, D. Brida, D. Polli, G. Cerullo, D.G. Lidzey, Phys. Rev. B **24**, 245309 (2011)
44. D.M. Coles, R.T. Grant, D.G. Lidzey, C. Clark, P.G. Lagoudakis, Phys. Rev. B **88**, 121303 (2013)
45. M. Sliotsky, Y. Zhang, S.R. Forrest, Phys. Rev. B **86**, 045312 (2012)
46. J.A. Ćwik, S. Reja, P.B. Littlewood, J. Keeling, Europhys. Lett. **105**, 47009 (2014)
47. P. Lagoudakis, Nature Mat. **13**, 227 (2014)
48. L. Fontanesi, L. Mazza, G.C. La Rocca, Phys. Rev. B **80**, 235313 (2009)
49. L. Mazza, L. Fontanesi, G.C. La Rocca, Phys. Rev. B **80**, 235314 (2009)

50. L. Mazza, S. Kéna-Cohen, P. Michetti, G.C. La Rocca, *Phys. Rev. B* **88**, 075321 (2013)
51. S. Kéna-Cohen, M. Davanço, S.R. Forrest, *Phys. Rev. Lett.* **101**, 116401 (2008)
52. S. Kéna-Cohen, Ph.D. thesis, Princeton University, 2010
53. A.E. Siegman, *Lasers* (University Science Books, Mill Valley, 1986)
54. M. Litinskaya, P. Reineker, V.M. Agranovich, *Phys. Stat. Solidi A* **201**, 646 (2004)
55. H. Zoubi, G.C. La Rocca, *Phys. Rev. B* **71**, 235316 (2005)
56. S. Kéna-Cohen, M. Davanço, S.R. Forrest, *Phys. Rev. B* **78**, 153102 (2008)
57. R.C. Powell, Z.G. Soos, *J. Lumin.* **11**, 1 (1975)
58. G.M. Akselrod, Y.R. Tischler, E.R. Young, D.G. Nocera, V. Bulovic, *Phys. Rev. B* **82**, 113106 (2010)
59. V.M. Agranovich, M. Litinskaya, G.C. La Rocca, D.G. Lidzey, in: *Organic Nanophotonics Nato Science Series II*, vol. 100, ed. by F. Charra, V.M. Agranovich, F. Kajzar (2003), p. 291
60. M. Litinskaya, P. Reineker, V.M. Agranovich, *J. Lumin.* **119**, 277 (2006)
61. H. Zoubi, G.C. La Rocca, *Phys. Rev. B* **72**, 125306 (2005)
62. M. Litinskaya, P. Reineker, V.M. Agranovich, *J. Lumin.* **110**, 364 (2004)
63. G.C. Morris, M.G. Sceats, *Chem. Phys.* **3**, 164 (1973)
64. R.J. Holmes, S.R. Forrest, *Phys. Rev. Lett.* **93**, 186404 (2004)
65. T.-S. Ahn, A.M. Müller, R.O. Al-Kaysi, F.C. Spano, J.E. Norton, D. Beljonne, J.-L. Brédas, C.J. Bardeen, *J. Chem. Phys.* **128**, 054505 (2008)
66. M. Hoffmann, Z.G. Soos, *Phys. Rev. B* **66**, 024305 (2002)
67. L.E. Lyons, L.J. Warren, *Aust. J. Chem.* **25**, 1411 (1972)
68. L. Silvestri, S. Tavazzi, P. Spearman, L. Raimondo, F.C. Spano, *J. Chem. Phys.* **160**, 234701 (2009)

Organic Nanophotonics

Fundamentals and Applications

Zhao, Y.S. (Ed.)

2015, X, 208 p. 116 illus., 47 illus. in color., Hardcover

ISBN: 978-3-662-45081-9